12-1-2011

Quantifying the Tibiofemoral Joint Space Using X-ray Tomosynthesis

Benjamin Kalinosky
Marquette University

John M. Sabol
GE Healthcare

Kelly Piacsek
GE Healthcare

Beth Heckel
GE Healthcare

Taly Gilat Schmidt
Marquette University, tal.gilat-schmidt@marquette.edu

Published version. *Medical Physics*, Vol. 38, No. 12 (December 2011): 6672-6682. DOI.

Quantifying the Tibiofemoral Joint Space Using X-Ray Tomosynthesis

Benjamin Kalinosky
Department of Biomedical Engineering, Marquette University
Milwaukee, WI
John M. Sabol
GE Healthcare
Waukesha, WI
Kelly Piacsek
GE Healthcare
Waukesha, WI
Beth Heckel
GE Healthcare
Waukesha, WI
Taly Gilat-Schmidt
Department of Biomedical Engineering, Marquette University
Milwaukee, WI

Abstract

Purpose: Digital x-raytomosynthesis (DTS) has the potential to provide 3D information about the knee joint in a load-bearing posture, which may improve diagnosis and monitoring of knee osteoarthritis compared with projection radiography, the current standard of care. Manually quantifying and visualizing the joint space width (JSW) from 3D tomosynthesis datasets

Medical Physics, Vol. 38, No. 12 (December 2011): pg. 6672-6682. DOI.

may be challenging. This work developed a semiautomated algorithm for quantifying the 3D tibiofemoral JSW from reconstructed DTS images. The algorithm was validated through anthropomorphic phantom experiments and applied to three clinical datasets.

Methods: A user-selected volume of interest within the reconstructed DTS volume was enhanced with 1D multiscale gradient kernels. The edge-enhanced volumes were divided by polarity into tibial and femoral edge maps and combined across kernel scales. A 2D connected components algorithm was performed to determine candidate tibial and femoral edges. A 2D joint space width map (JSW) was constructed to represent the 3D tibiofemoral joint space. To quantify the algorithm accuracy, an adjustable knee phantom was constructed, and eleven posterior–anterior (PA) and lateral DTS scans were acquired with the medial minimum JSW of the phantom set to 0–5 mm in 0.5 mm increments (VolumeRad™, GE Healthcare, Chalfont St. Giles, United Kingdom). The accuracy of the algorithm was quantified by comparing the minimum JSW in a region of interest in the medial compartment of the JSW map to the measured phantom setting for each trial. In addition, the algorithm was applied to DTS scans of a static knee phantom and the JSW map compared to values estimated from a manually segmented computed tomography(CT) dataset. The algorithm was also applied to three clinical DTS datasets of osteoarthritic patients.

Results: The algorithm segmented the JSW and generated a JSW map for all phantom and clinical datasets. For the adjustable phantom, the estimated minimum JSW values were plotted against the measured values for all trials. A linear fit estimated a slope of 0.887 ($R^2 = 0.962$) and a mean error across all trials of 0.34 mm for the PA phantom data. The estimated minimum JSW values for the lateral adjustable phantom acquisitions were found to have low correlation to the measured values ($R^2 = 0.377$), with a mean error of 2.13 mm. The error in the lateral adjustable-phantom datasets appeared to be caused by artifacts due to unrealistic features in the phantom bones. JSW maps generated by DTS and CT varied by a mean of 0.6 mm and 0.8 mm across the knee joint, for PA and lateral scans. The tibial and femoral edges were successfully segmented and JSW maps determined for PA and lateral clinical DTS datasets.

Conclusions: A semiautomated method is presented for quantifying the 3D joint space in a 2D JSW map using tomosynthesisimages. The proposed algorithm quantified the JSW across the knee joint to sub-millimeter accuracy for PA tomosynthesis acquisitions. Overall, the results suggest that x-raytomosynthesis may be beneficial for diagnosing and monitoring disease progression or treatment of osteoarthritis by providing quantitative images of JSW in the load-bearing knee.

Medical Physics, Vol. 38, No. 12 (December 2011): pg. 6672-6682. DOI.

Introduction

Osteoarthritis is the most common cause of disability in the United States, affecting 46 million people in the US alone, including half of the population over 65.[1] Knee osteoarthritis is a prevalent condition that progresses in pain and disability in late age, thus the impact of this disease on the economy is expected to increase with the aging baby boomer population.[1] As life expectancy increases, osteoarthritis is also expected to affect a rising proportion of the population throughout the future.[2]

Managing the symptoms of osteoarthritis is possible with early diagnosis and treatment. The Kellgren-Lawrence[2] grading system, based on radiographic images of the knee, is a gold standard for diagnosing and staging the severity of osteoarthritis.[3] This method considers joint space narrowing (JSN), subchondral sclerosis, and osteophytosis in grading the severity of osteoarthritis. JSN is a common clinically-used criterion for diagnosing knee osteoarthritis and is determined by measuring the minimum joint space width (JSW) in both the medial and lateral compartments of the knee joint from projection radiographs.[2,4]

Clinically, the JSW is measured from a radiograph by manually marking the location where the tibia and femur appear to be closest.[3–6] Kijowski et al.[4] found the sensitivity and specificity of JSN in detecting degeneration of articular cartilage to be 46 and 95% in the medial compartment and 7 and 100% in the lateral compartment, respectively. Previous studies found that computerized JSW measurements in the medial and lateral knee compartments were more precise, accurate, and reproducible.[7–9] Shamir et al.[10] proposed an automated method using features of a 2D X-ray image to determine the equivalent grade on the Kellgren-Lawrence scale. Duryea et al.[11] introduced a trainable rule-based algorithm for measuring JSW in projection knee radiographs.

The limited information provided in 2D projection radiographs leads to subjective and variable measurements and diagnosis.[12] Since JSW is a 2D measurement in a radiograph, quantifying the true 3D distance and location is a challenge. Measures of severity from knee radiographs are also highly sensitive to joint positioning, which has

Medical Physics, Vol. 38, No. 12 (December 2011): pg. 6672-6682. DOI.

been found difficult to reproduce, especially in patients presenting with pain and limited joint mobility.[12] MRI and CT may overcome these limitations by providing structural and 3D information not found in x-ray projections. The use of MRI for knee imaging is increasing due to its high soft-tissue contrast, which enables sensitive joint imaging.[13,14] Both CT and MRI are more expensive and time consuming than x-ray radiographs, potentially increasing the cost of OA treatment. While open-bore MRI systems have been used for knee imaging,[15,16] conventional MRI and CT systems cannot image the knee in a standing posture.

Digital tomosynthesis (DTS) is an x-ray imaging modality that acquires a series of projection radiographs over a limited angular range and allows for the reconstruction of an arbitrary number of 2D image slices through a 3D volume.[13–15] The application of tomosynthesis imaging has been proposed for imaging the breast, lung, and musculoskeletal applications, including arthritis in the hand.[17–21] DTS overcomes the limitations of projection x-ray imaging by removing overlying anatomy and providing anisotropic (high resolution in-plane and low resolution out-of-plane) 3D information of the knee joint in load-bearing posture. This information can help characterize the tibiofemoral joint space throughout the joint. As an example, Figure 1 illustrates how the ability to detect pathology consistent with symptoms of osteoarthritis and knee pain (a free floating bone chip) is improved with tomosynthesis as a result of the removal of overlying anatomic structure.

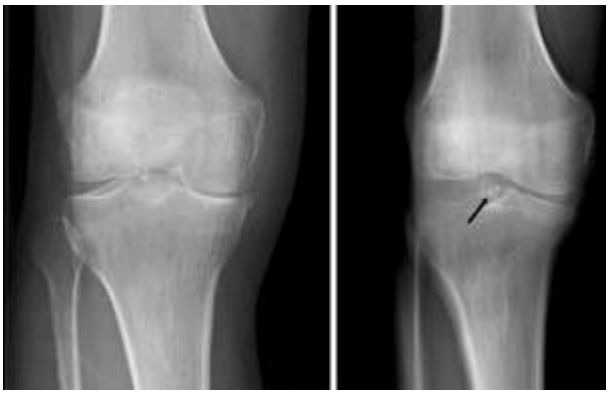

FIG. 1. Routine PA radiograph (left) and reconstructed tomosynthesis image (right) of the same patient. As a result of the effective removal of out-of-plane structures, a free-floating bone chip (arrow) is easier to visualize in the tomosynthesis slice image. (Images courtesy Dr. A. Guermazi, Boston Medical Center)

Medical Physics, Vol. 38, No. 12 (December 2011): pg. 6672-6682. DOI.

Manual quantification of the minimum JSW from 3D tomosynthesis datasets may be challenging due to the multiple reconstructed slices. Although computer-aided methods continue to be developed for analyzing knee radiographs and MRI images,[10,11,22,23] these tools do not yet exist for x-ray tomosynthesis, a modality with unique challenges due to anisotropic resolution and tomosynthesis artifacts. This paper introduces a semiautomated method for measuring the JSW throughout the knee joint from reconstructed tomosynthesis slices. The method requires the user to select a region of interest (ROI) containing the knee joint in one tomosynthesis slice, and is otherwise automated. The result is a 2D map of the JSW, which may be useful for diagnosing and staging osteoarthritis. Section II introduces the knee anatomy relevant to this paper and describes the proposed algorithm and validation study. The results of the validation study are presented in Sec. III, followed by a discussion of these results and potential applications.

Methods and Materials

Our aim was to characterize the 3D JSW from lateral and posterior–anterior (PA) sets of reconstructed DTS slices. Due to the unique properties of DTS images, segmentation algorithms proposed for x-ray and MRI knee images are not directly applicable. For example, the anisotropic resolution of DTS limits the effectiveness of the multidimensional edge enhancement, active contour, and shape modeling methods used in previously proposed segmentation algorithms.[11,22,23] Tomosynthesis images contain artifacts of ghost features from neighboring slices, thus requiring additional steps to differentiate true edges from artifacts. Furthermore, tomosynthesis images have limited soft-tissue contrast compared to MRI images, precluding the use of previously proposed cartilage segmentation algorithms.[23]

II.A. Anatomy

With respect to the joint space, the human knee is divided into medial and lateral compartments, as shown in Fig. 2. The joint space in each compartment is the region between the bottom surface of the femoral condyle and the top surface of the tibial plateau.

Medical Physics, Vol. 38, No. 12 (December 2011): pg. 6672-6682. DOI.

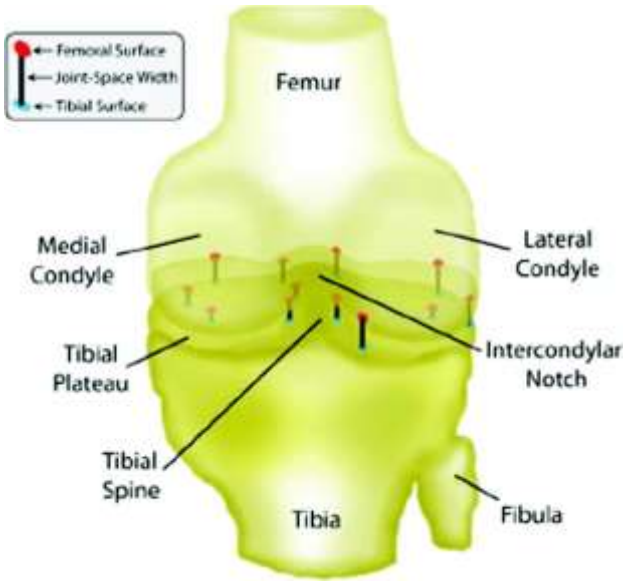

FIG. 2. Schematic drawing of the knee joint, compartments, and the tibiofemoral joint space.

When the knee bends, the articular cartilage slides against the meniscus. Thus, the thickness of the meniscus and articular cartilage, which determines the minimum joint space in each compartment, is dependent upon the knee angle. In this work we define the JSW as the vertical distance between the femoral and tibial surfaces.

II.B. Algorithm details

Steps of the proposed, semiautomated algorithm for segmenting and quantifying the tibiofemoral JSW are summarized in Fig. 3. As in the 2D algorithm developed for radiographs by Duryea et al.,[11] our proposed algorithm consists of edge-enhancement of a user-selected ROI followed by edge segmentation through connected component analysis. Our algorithm developed novel implementations of these steps in order to address the specific challenges of tomosynthesis.

Medical Physics, Vol. 38, No. 12 (December 2011): pg. 6672-6682. DOI.

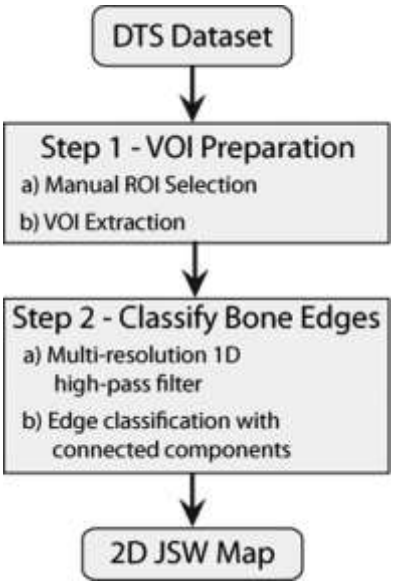

FIG. 3. Overview of semiautomated algorithm for calculating the JSW map.

II.B.1. Step 1—extract volume of interest (VOI)

Before segmenting the knee joint space, an ROI encompassing the knee joint was manually selected in one reconstructed tomosynthesis slice. Ideally, the 2D ROI extends above the intercondylar notch and below the tibial plateau, while encompassing the full transverse extent of the joint space. An example ROI is depicted in Fig. 4. A 3D volume of interest was then defined by extracting the selected 2D ROI in all slices.

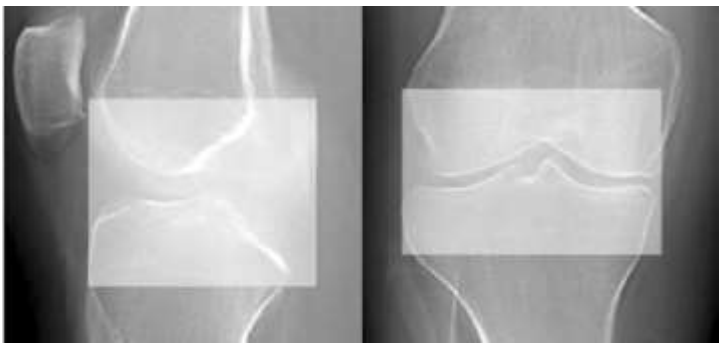

FIG. 4. ROI selection for (left) sagittal and (right) coronal reconstructed tomosynthesis images resulting from lateral and PA tomosynthesis acquisitions, respectively.

Medical Physics, Vol. 38, No. 12 (December 2011): pg. 6672-6682. DOI.

II.B.2. Step 2—classify bone edges

Step 2a: Multiresolution 1D High-pass filter

To enhance horizontal edges, the VOI was convolved with 1D high-pass kernels, oriented along the axial direction. Unlike the previous method that used a 2D Sobel filter,[11] 1D convolution was chosen to reduce sensitivity to tomosynthesis artifacts and variable edge orientation.

Fifteen 1D high-pass kernels of length 3 to 31 pixels (0.6–6.2 mm) were generated by taking the first derivative of Gaussian functions with standard deviation, σ_n, increasing from 0.5 to 6.0 mm, respectively. These kernels are the same as those used in the Canny edge detection method.[24] The maximum standard deviation of 6.0 mm was selected as an approximation of the average healthy adult minimum JSW. Let vector $\mathbf{k}n$ be the nth kernel with $n \in \{1,2,\ldots,15\}$. The length of $\mathbf{k}_n$ is $L_n=1+2n$. The ith element of $\mathbf{k}_n$, denoted as $k_{n,t}$, is defined as

$$k_{n,i} = \frac{k'_{n,i}}{\sum_{j=1}^{L_n} |k'_{n,j}|} \tag{1}$$

$$k'_{n,i} = \frac{-z_i}{\sqrt{2\pi}\sigma_n} e^{-\frac{z_i^2}{2}} i \in \{0, 1, \ldots, L_n - 2, L_n - 1\} \tag{2}$$

with standard deviation and

$$z_i = \frac{i - n}{\sigma_n} \tag{3}$$

The resulting gradient kernels, plotted in Fig. 5 for lengths 3, 9, and 31, enabled the enhancement of both the tibial and femoral edges with opposite polarity in a single convolution. The multiresolution kernels were designed to match edges of varying thicknesses, which is necessary in tomosynthesis due to decreased spatial resolution toward the edges of the reconstructed volume. As the standard deviation decreases, the kernel approaches a central difference approximation, i.e., k1 = {−0.5, 0.0, 0.5}, as seen in Fig. 5.

Medical Physics, Vol. 38, No. 12 (December 2011): pg. 6672-6682. DOI.

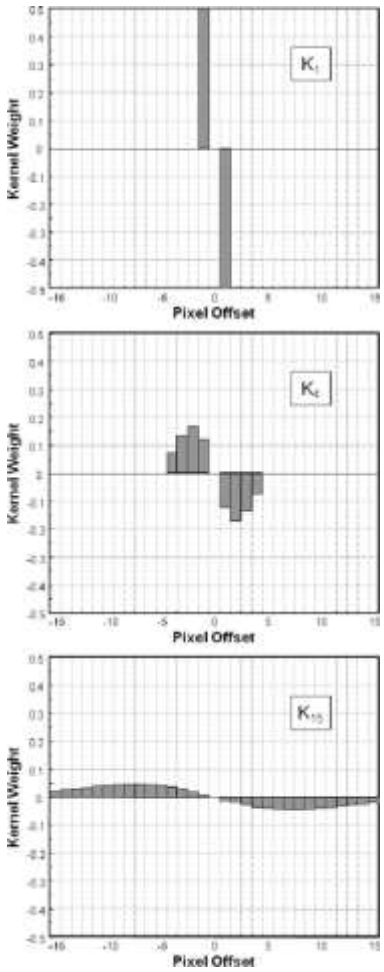

FIG. 5. High-pass kernels of length 3 (K_1), 9 (K_5), and 31(K_{15}) representing the first derivative of a Gaussian function. Kernels of length 3 to 31 were used to enhance the tibiofemoral space margins.

Longer gradient kernels were observed to enhance the tibiofemoral joint space margins while being less sensitive to features such as to bone texture, osteophytosis, and intra-JSW features (e.g. anterior and posterior cruciate ligaments) compared to the shorter kernels. However, longer kernels resulted in a spreading of the edge features, making it difficult to identify the true edge location. The shorter gradient kernels provided more precise localization of the edges, while being more sensitive to spurious edge features. The goal of the algorithm was to combine the information resulting from all multiresolution kernels to localize the tibial and femoral edges.

Medical Physics, Vol. 38, No. 12 (December 2011): pg. 6672-6682. DOI.

The determination of edge candidates was performed on a column-by-column basis, where the columns span the axial direction. To explain the algorithm, let **c** represent a column in the VOI. The column was first convolved with each gradient kernel $\mathbf{k}_n$ to give 15 edge-enhanced vectors $\mathbf{q}_n$:

$$q_n = \mathbf{c} * k_n \tag{4}$$

The mean, $\overline{\mathbf{q}}_n$, and standard deviation, $std(\mathbf{q}_n)$, of each of the 15 edge enhanced vectors were calculated. Fifteen binary vectors $\mathbf{t}_n$ were defined to mask the location of candidate tibial edges in the corresponding edge enhanced vectors $\mathbf{q}_n$. The ith element of mask vector $\mathbf{t}_n$ was assigned a value of one if the ith element of $\mathbf{q}_n$ was more than 1.5 standard deviations below the mean of $\mathbf{q}_n$, as described in Eq. (5). Similarly, fifteen binary vectors $\mathbf{f}_n$ were defined to mask candidate femoral edges at locations where the values of $\mathbf{q}_n$ were more than 1.5 standard deviations above the mean, as described in Eq. (6).

$$t_{n,j} = \begin{cases} 1 & q_{n,j} < (\bar{q}_n - 1.5.std(q_n)) \\ 0 & \text{otherwise} \end{cases} \tag{5}$$

$$f_{n,j} = \begin{cases} 1 & q_{n,j} < (\bar{q}_n - 1.5.std(q_n)) \\ 0 & \text{otherwise} \end{cases} \tag{6}$$

The mask vectors, $\mathbf{t}_n$ and $\mathbf{f}_n$, resulting from the 15 kernel widths were weighted and summed to create a cumulative edge map, **T** for the candidate tibial edges and **F** for the candidate femoral edges, as described in Eqs. (7) and (8). As shown in Fig. 5, the gradient kernels become more similar as kernel length and *n* increase. Therefore, the information contained in the edge mask is more redundant as *n* increases. To compensate for this, the heuristic weighting scheme described in Eqs. (7) and (8) was chosen to increase weight with decreasing kernel length to account for redundant edge information in longer kernels.

Medical Physics, Vol. 38, No. 12 (December 2011): pg. 6672-6682. DOI.

$$\mathbf{T} = \sum_{n=1}^{15} \mathbf{t}_n \cdot exp\left(-2\pi \frac{n}{15}\right) \tag{7}$$

$$\mathbf{F} = \sum_{n=1}^{15} \mathbf{f}_n \cdot exp\left(-2\pi \frac{n}{15}\right) \tag{8}$$

Overall, the tibial and femoral edge maps, **T** and **F**, contained high values at the pixel locations that were identified as edge candidates by multiple resolution kernels, with more weight given to edges identified by the shorter kernels. Therefore, pixels in the edge maps **T** and **F** with high value were more likely to represent edges.

Step 2b: Edge Classification with Connected-Components

The tibial and femur edge maps **T** and **F** were each median filtered with a 5×5 neighborhood in order to increase edge coherence between columns, thresholded to unity for values greater than 10% of the maximum, and labeled with a connected-components algorithm using 4-connectivity. The resulting labeled components contained the tibial and femoral edges as well as numerous smaller edges due to normal bone structure and noise.

The resulting edges were classified by analyzing the features of the labeled components. One feature was derived from the observation that the tibial and femoral components were primarily oriented in the horizontal direction. Thus, an edge candidate was rejected if the width to height ratio of its bounding box was less than one. The second feature was based on the assumption that the tibial and femoral edges were expected to be the largest connected components. In each slice, connected components below the 95th percentile of connected component sizes were rejected. This threshold was typically between 20 and 40 pixels (0.8–1.6 mm^2).

In the previously proposed algorithm for radiographs,[11] edge components were classified according to average grayscale value, however this criteria was not successful for the DTS data. Instead, the femoral edge component was identified in each column as the largest of the connected components remaining after morphological filtering.

Medical Physics, Vol. 38, No. 12 (December 2011): pg. 6672-6682. DOI.

Next, the largest connected component inferior to the femoral component was chosen as the tibial component.

Once the tibial and femoral edge components were identified, the next step was to determine the edge locations within the components. The edge maps, **T** and **F**, whose values represent the 'likelihood' of being an edge, exhibited a trapezoidal profile along the columns within each edge component. To determine the femoral edge location, the derivative of edge map **F** within the selected component was calculated by finite difference within each column. In each column, the location of the femoral edge was chosen as the pixel with the most negative derivative. This can be thought of as the most inferior pixel in the component with a high cumulative score for being an edge. The tibial edge was localized using a similar procedure.

II.B.3. Step 3—quantify joint space width

For each pixel location in the transverse plane, the JSW was calculated as the difference between the estimated axial locations of the tibial and femoral edges. This distance between the two edges was represented by a 2D JSW map for visualization. For example, if the number of slices in the tomosynthesis datasets was *K*, and the ROI selected in Step 1 had a width of *N* columns and height of *Q* rows, the resulting JSW map was a *K* by *N* image, with each pixel in the JSW map representing the vertical distance between the tibial and femoral edges at that transaxial location in the knee joint.

II.C. Experimental validation

The algorithm was implemented in JAVA 6.0. The validation workstation was an HP HDX 18t, Intel® Core™2 Extreme CPU Q9300 @ 2.53 GHz, 4.00 GB DDR3-RAM, Windows 7 Professional 64-bit. The slices of each processed dataset were distributed to four threads for edge enhancement and classification.

II.C.1. Tomosynthesis protocol

Tomosynthesis acquisitions were performed on the Definium8000 with VOLUMERAD software (GE Healthcare, Chalfont St Giles, England). Using the tomosynthesis acquisition technique, 40

projection images were acquired over a 40° arc with approximately one-degree angular spacing. Both PA and lateral sweeps were performed. The source-to-image distance was 180 cm for the central projection. Each projection image was acquired at 70 kVp and approximately 1.25 mAs resulting in an incident air kerma of approximately 0.1 mGy. A modified filtered backprojection algorithm[25] reconstructed the tomosynthesis dataset into 66 tomosynthesis slice images parallel to the detector plane with 0.2×0.2 mm in-plane pixel pitch and 2 mm pitch between slices.

All reconstructed DTS datasets were input to the proposed algorithm, with the user selecting the ROI in the central reconstructed slice as described in Sec. ???. The proposed algorithm output a 2D JSW map with 66 rows and a number of columns equal to the width of the manually selected ROI.

II.C.2. Knee phantom studies

An adjustable knee phantom was developed to provide a known minimum JSW against which to validate the algorithm, as pictured in Fig. 6(a). The phantom represented a typical adult right knee, comprised of x-ray equivalent femur and tibia phantoms (Model LS-160-RO, Aptic Superbones, Vashon, WA). The phantom was constructed of durable rigid polyurethane foam with a special radiopaque material infused into the model. The radiopaque material was not uniformly dispersed throughout the foam, rather had the appearance of a dispersion of a radiopaque precipitate suspended in the foam. Thus this phantom provided a highly realistic anthropomorphic characterization of the shape of knee joint, but on a small scale did not provide x-ray attenuation representative of actual bones. More specifically, the phantom bones contained very small focal points of attenuation surrounded by the relatively nonattenuating foam as can be seen in Fig. 6(b). The femur was secured with two vertically aligned clamps mounted on a linear slide bearing to allow adjustment of the joint space. The elevation of the clamp, and hence the femur, was adjustable to 0.03-mm precision with a fine gauge and output dial as shown in Fig. 6(a).

Medical Physics, Vol. 38, No. 12 (December 2011): pg. 6672-6682. DOI.

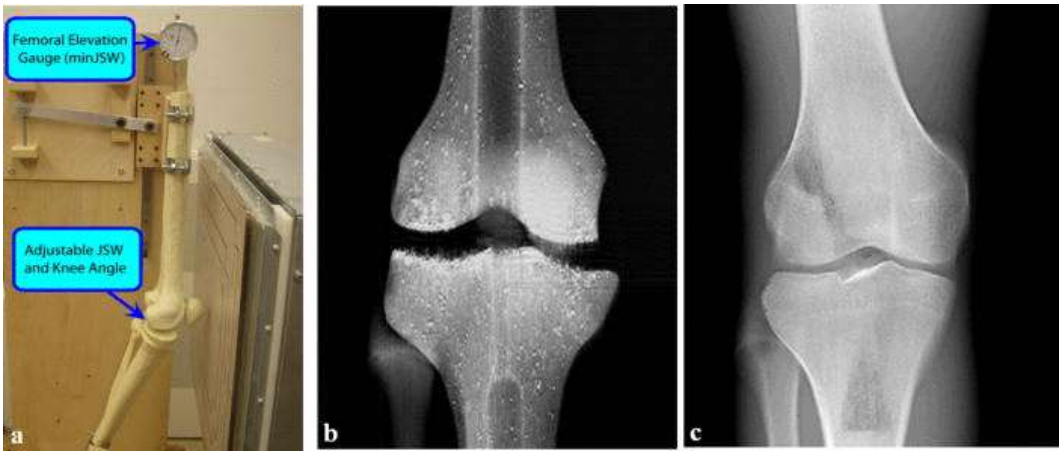

FIG. 6. (a) Adjustable knee phantom. (b) Typical mid-coronal slice from a reconstructed PA tomosynthesis acquisition of the adjustable knee phantom. (c) Typical mid-coronal slice from a reconstructed PA tomosynthesis acquisition of the static knee phantom.

DTS acquisitions were performed to evaluate the accuracy of the minimum JSW (minJSW) estimated by the algorithm compared to the known minJSW measured in the phantom. In each set of experiments, the angle of the phantom knee joint was held constant at 0 degrees and the fine gauge was first calibrated to 0.0 mm after adjusting the femur such that it came into contact with the tibia in the medial compartment, representing a minJSW of 0 mm. For each DTS acquisition type (PA and lateral), eleven tomosynthesis scans were acquired with the gauge increased by 0.5 mm between scans, resulting in minJSW values of 0.00 to 5.00 mm in 0.5 mm increments. In the resulting JSW maps, the minJSW was estimated as the minimum value within a manually selected 11×200 pixel (22×40 mm) ROI within each JSW map. The accuracy of the algorithm was evaluated by plotting the estimated minJSW of the phantom image against the measured minJSW. In addition, the mean absolute error of the minJSW was calculated across all trials for each type of DTS acquisition.

The adjustable knee phantom provided validation at one location in the tibiofemoral joint space. However, tomosynthesis artifacts increase towards the edges of the FOV. To verify the performance of the algorithm across the knee joint, a static knee phantom containing dry human bones in an extended position (XA245L, Phantom Lab,

Medical Physics, Vol. 38, No. 12 (December 2011): pg. 6672-6682. DOI.

Salem NY) was scanned with both the tomosynthesis protocol and by CT (Lightspeed VCT, GE Healthcare, Chalfont St Giles, England) at 120 kVp, 100 mA, and a helical pitch of 0.53. Figure 6(c) displays a reconstructed tomosynthesis slice of the static phantom. CT images of the static phantom were reconstructed with the boneplus kernel onto a volume of $512 \times 512 \times 278$ voxels of dimension $0.25 \times 0.25 \times 0.625$ mm. A JSW map was generated from the DTS dataset by the semi-automated algorithm, independently of the CT data. The CT and DTS datasets were acquired with the phantom in different orientations and were reconstructed onto different coordinate systems and sampling grids. In order to enable comparison of JSW maps generated from the DTS and CT datasets, the reconstructed CT volume was registered to each of the reconstructed PA and lateral DTS volumes. Rigid body transformations were estimated by a nonlinear least squares algorithm using nine anatomical features manually selected in each dataset. After registration, the tibiofemoral joint space margins were manually segmented on reformated coronal and sagittal CT images. The resulting CT JSW maps were resampled to the coordinates of the DTS maps using bicubic interpolation and the difference between the DTS and CT maps calculated.

II.C.3. Clinical datasets

Clinical tomosynthesis datasets were acquired from an ongoing clinical trial conducted under approval of an institutional review board. All patients granted their informed consent and were informed that the image data may be used for further analysis. Three deidentified datasets of knee osteoarthritis patients were used to demonstrate preliminary feasibility of the algorithm for clinical data. The PA and lateral clinical scans were acquired with the patient standing and maintaining an approximate 20° knee flexion angle with the aid of a positioning device[7] (SynaFlexer™, Synarc Inc., San Francisco, CA). Two of the clinical datasets included PA and lateral acquisitions of the same patient, while the third dataset was from a lateral acquisition of a second patient.

Medical Physics, Vol. 38, No. 12 (December 2011): pg. 6672-6682. DOI.

Results

The algorithm processed 22 phantom datasets in 44 minutes and 56 seconds (15.49% of this time was spent reading and extracting the VOI's from the DICOM files). The calculation time was 10.220 ± 0.524 s per million voxels processed across all phantom datasets.

III.A. Knee phantom studies

Figures 7 and 8 display the intermediate output of steps 2a and 2b of the proposed algorithm applied to the adjustable phantom images, including (a) the candidate tibial and femoral edge maps, (b) the filtered connected components for each edge map and (c) the localized tibial and femoral edges on one reconstructed slice image of the phantom. Figure 9 displays JSW maps output by the algorithm for PA and lateral acquisitions of the adjustable and static phantoms. Each pixel in the JSW map represents the vertical distance between the tibial and femoral edges at the corresponding transverse location in the knee joint.

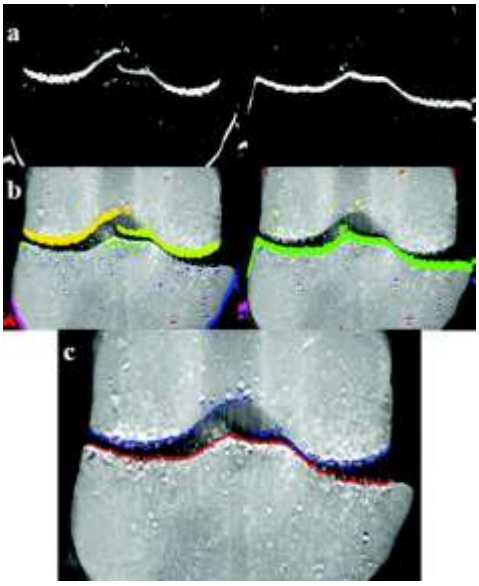

FIG. 7. (a) Femoral (left) and tibial (right) edge probability maps (F and T) for the mid-coronal slice of a PA phantom dataset. (b) The labeled edge components after morphological filtering. (c) A mid-coronal slice from a PA phantom dataset with the computed joint space margins for the tibia (red) and femur (blue).

Medical Physics, Vol. 38, No. 12 (December 2011): pg. 6672-6682. DOI.

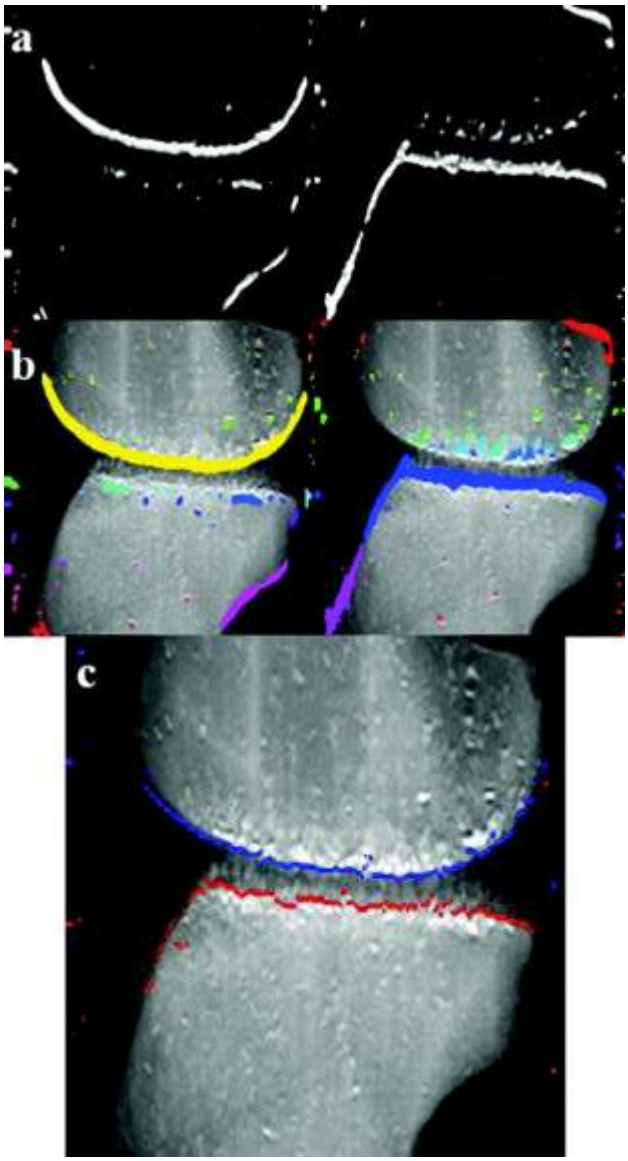

FIG. 8. (a) Femoral (left) and tibial (right) edge probability maps (F and T) for the mid-sagittal slice of a lateral phantom dataset. (b) The labeled edge components after morphological filtering. (c) A mid-sagittal slice from a lateral phantom dataset with the computed joint space margins for the tibia (red) and femur (blue).

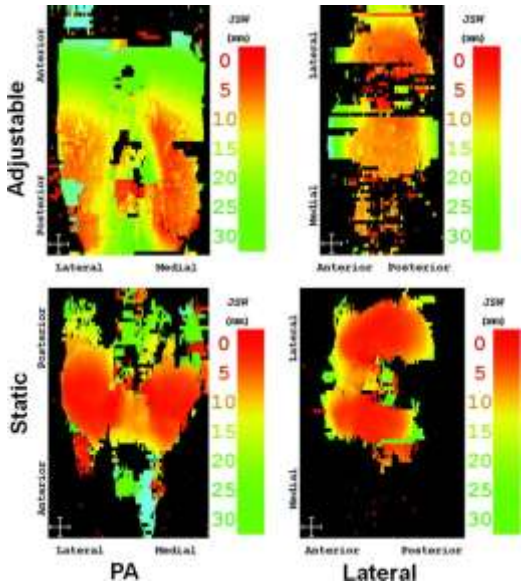

FIG. 9. The JSW maps computed from 66 reconstructed tomosynthesis slices for PA (left) and lateral (right) acquisitions of the adjustable phantom (5 mm minJSW) and static phantom. The white cross-hair cursor depicts a 1 cm^2 area.

Figures 10 and 11 display the estimated minJSW plotted against the minJSW values measured on the knee phantom for the PA and lateral sweeps of the adjustable phantom. The ideal relationship between the calculated and measured values is also shown. The estimated minJSW values were highly correlated to the true vales for the PA datasets ($R^2 = 0.962$), but not for the lateral datasets ($R^2 = 0.377$). The mean error across all trials was 0.34 mm for the PA experiments and 2.13 mm for the lateral experiments. Figure 12 displays an example of a lateral reconstructed image where the algorithm failed to identify the correct edges. As displayed in Fig. 12, speckles and artifacts from features in surrounding slices compromised the vertical joint-space contrast.

Medical Physics, Vol. 38, No. 12 (December 2011): pg. 6672-6682. DOI.

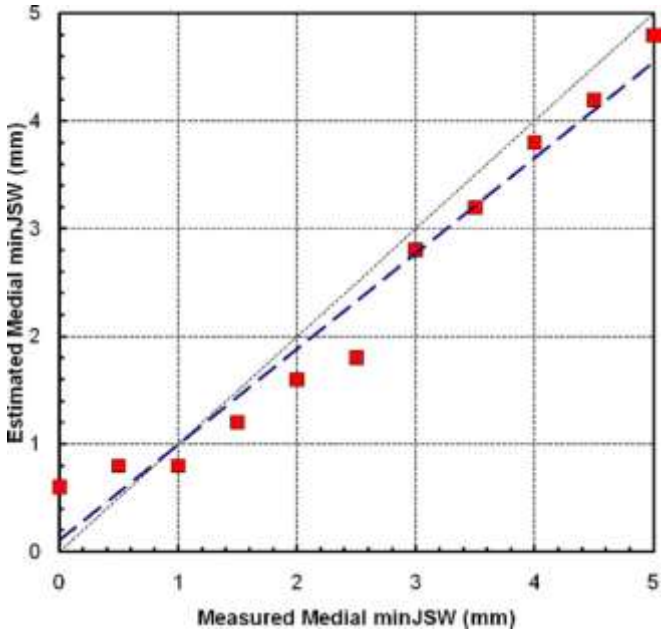

FIG. 10. The medial minJSW measured by the phantom versus the medial minJSW estimated by the algorithm for all PA trials (square data points). For reference, a linear fit to this data (dashed line) and the unity line (dotted) representing ideal estimation of minJSW are also plotted.

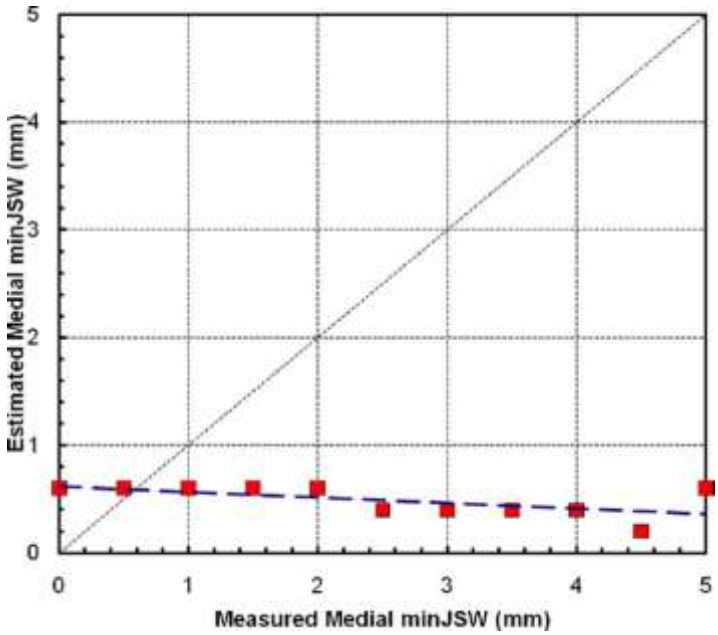

FIG. 11. The medial minJSW measured by the phantom versus the medial minJSW estimated by the algorithm for all lateral trials (square data points). For reference, a linear fit to this data (dashed line) and the unity line (dotted) representing ideal estimation of minJSW are also plotted.

Medical Physics, Vol. 38, No. 12 (December 2011): pg. 6672-6682. DOI.

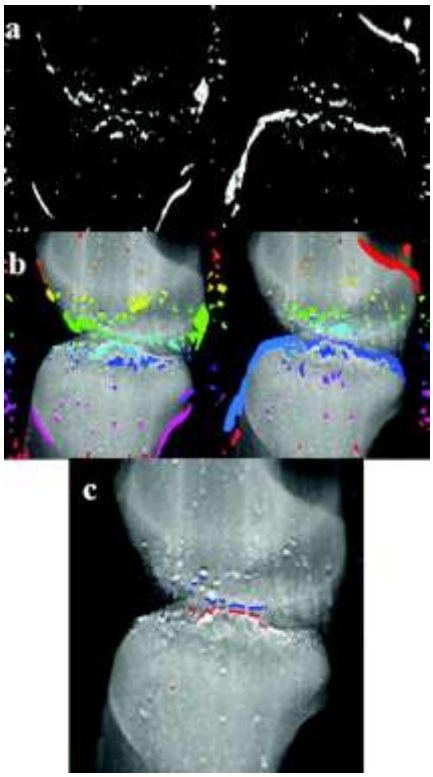

FIG. 12. (a) Femoral (left) and tibial (right) edge probability maps (F and T) for the mid-sagittal slice of a lateral phantom dataset where the tibial and femoral edges were not successfully located. (b) The labeled edge components after morphological filtering. (c) A mid-sagittal slice from a lateral phantom acquisition with the computed joint space margins for the tibia (red) and femur (blue).

The difference between JSW maps calculated by the algorithm for DTS images and by manual segmentation of CT images is displayed in Figs. 13 and 14 for PA and lateral acquisitions, respectively. Representative horizontal profiles through the JSW maps are also plotted. The mean and median absolute difference between valid pixels of the DTS and CT maps was 0.67 and 0.51 mm for the PA data and 0.81 and 0.60 mm for the lateral data. The largest differences were generally located at the boundaries of the map. The reported numbers represent the difference between the CT and DTS-generated JSW maps, but not necessarily the error, as the CT JSW map also contained errors. The slice thickness in the reconstructed CT volume was 0.625 mm, therefore manual segmentation errors due to partial volume artifacts could be on order millimeters. Additional error may be introduced during registration of the DTS and CT volumes. Overall, the results of the adjustable phantom quantify the absolute error for a

single known point, while the results of the static phantom demonstrate that this error is generally consistent across the joint space.

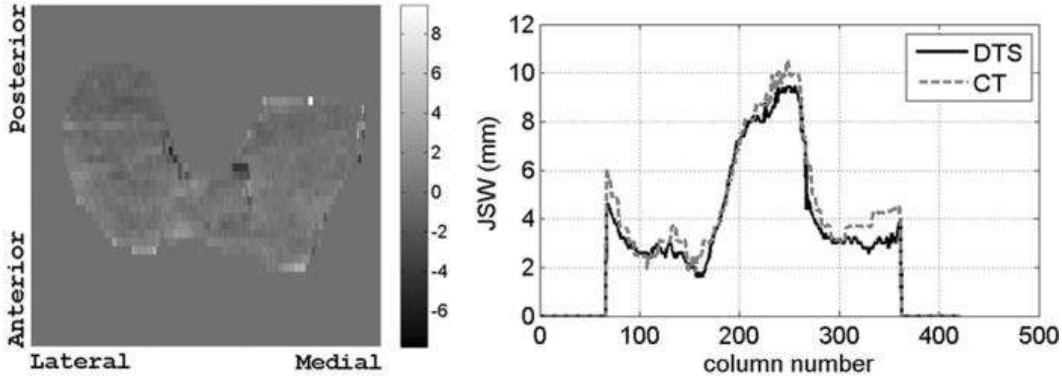

FIG. 13. (left) The difference in millimeters between JSW maps calculated by the algorithm from PA tomosynthesis images and by manually segmented CT images of the static phantom. (right) Comparison of a horizontal profile through the JSW maps.

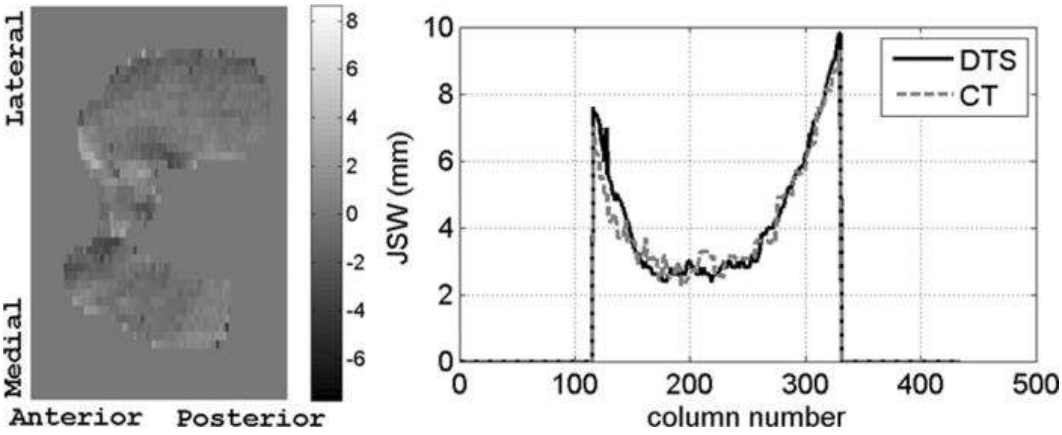

FIG. 14. (left) The difference in millimeters between JSW maps determined by the algorithm from lateral tomosynthesis images and by manually segmented CT images of the static phantom. (right) Comparison of a horizontal profile through the JSW maps.

III.B. Clinical datasets

Figure 15 displays reconstructed tomosynthesis slice images from clinical PA and lateral acquisitions along with the tibial and femoral edges determined by the algorithm. The 2D JSW maps resulting from analysis of all slice images are also displayed. In both

Medical Physics, Vol. 38, No. 12 (December 2011): pg. 6672-6682. DOI.

PA and lateral cases, the algorithm identified the joint space margins in all slices and created a JSW map. These JSW maps illustrate that the proposed algorithm in combination with a tomosynthesis acquisition enables visualization of potential joint space narrowing throughout the entire joint previously accessible only with 3D imaging techniques such as CT and MRI.

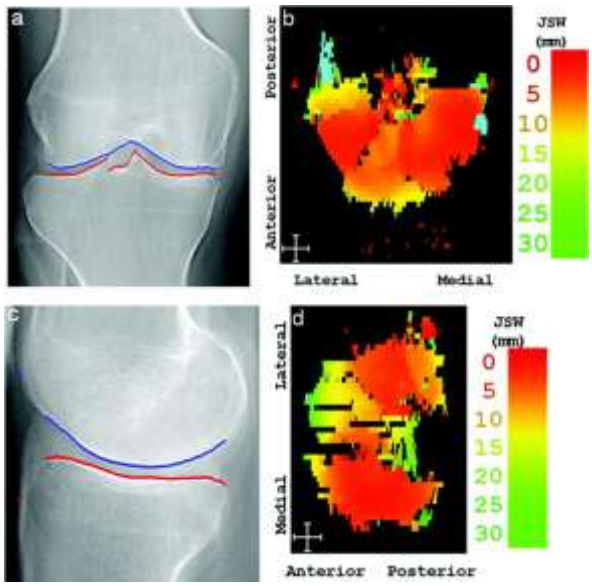

FIG. 15. (a) The computed joint space margins for the tibia (red) and femur (blue) in a mid-coronal slice from a PA sweep of a knee with clinical osteoarthritis and (b) the derived 2D JSW map. (c) The computed joint space margins in a mid-sagittal slice from a lateral sweep of a knee with clinical osteoarthritis and (d) the derived 2D JSW map. The white cross-hair cursor depicts a 1 cm^2 area.

Discussion and Conclusions

This study investigated the feasibility of visualizing and quantifying the knee JSW using DTS imaging. The results indicate that the proposed algorithm is able to segment the tibial and femoral edges and quantify the absolute minimum JSW to an accuracy of ~0.34 mm for tomosynthesis images resulting from a PA sweep. Results of the CT validation suggest that the sub-millimeter error is generally consistent across the joint. Since tomosynthesis imaging will minimize the impact of superposition found in radiographs, the proposed algorithm has the potential to reduce the impact of high observer variability in assessing JSW from radiographs[8,9] and improve accuracy and consistency in determination of minJSW. Further research is required to investigate if

Medical Physics, Vol. 38, No. 12 (December 2011): pg. 6672-6682. DOI.

optimization of the acquisition and reconstruction parameters (for example decreasing the distance between reconstructed slices) would improve edge detection in the tomosynthesis image sets.

Figures 9 and 10 demonstrate that while the estimated and measured minJSW are strongly correlated for the PA phantom, the results from the lateral datasets show relatively high error (~2 mm) and poor correlation ($R^2 = 0.377$). When the knee anatomy is reconstructed on sagittal slices, as in the lateral tomosynthesis datasets, the tibial and femoral edges change more rapidly between slices than in coronal slices (see knee anatomy in Fig. 2). This rapid change reduces the contrast of edges within the tomosynthesis slice images thereby increasing sensitivity to speckles. Note that this issue does not manifest in the more realistic static phantom, for which the algorithm performed similarly for lateral and PA datasets.

The algorithm was tested on three clinical tomosynthesis datasets, two of which included lateral acquisitions. The algorithm correctly identified the tibial and femoral edges in all slices of the clinical data. Therefore, the results suggest that the algorithm will have improved performance for clinical lateral datasets compared to the results obtained with the adjustable phantom. Overall, Fig. 15 demonstrates preliminary feasibility of quantifying the JSW in clinical datasets. Although the geometric accuracy of tomosynthesis has been quantified in both phantom and clinical imaging,[26,27] future work is required to validate the clinical performance of this algorithm by comparing the output to measurements from trained observers on patients presenting with a range of OA disease severity.

Several additional improvements may increase the clinical utility of the presented algorithm. First, the selection of the ROI enclosing the knee joint could be automated by registering the dataset with an averaged image of the joint center, similar to the method proposed by Shamir et al.,[10] in order to reduce variability due to manual selection. A second possible improvement is automated segmentation of the medial and lateral compartments within the JSW map and automated identification the minimum JSW within each compartment. The detection of zero joint space width is another necessary improvement to the algorithm since bone-on-bone contact is a situation that occurs and is of high clinical significance with OA. Currently, the use of the

smallest gradient kernel size assumes that there is at least one pixel of space between the femur and tibia for all columns. The event of zero JSW may be detected by a follow-up process to the current algorithm that applies separate spline fits to the tibial and femoral edges surrounding the point of zero joint space. The location of bone contact could then be estimated as the point where the distance between two fitted curves is minimized or is below a predetermined threshold value. Another possible improvement in the algorithm is support for DTS datasets that include both knees of the subject. First, a knee joint must be determined to be from the subject's left or right leg which could be accomplished by detecting the location of the fibula. Second, the proposed method could be applied separately to two ROI's enclosing each knee joint in the dataset.

The use of morphometric analysis of bone trabecular structure has been investigated as a biomarker of the presence, severity, and progression of OA.[28,29] A texture based, morphometric analysis may be more accurate with tomosynthesis than standard projection imaging due to the lack of superimposed structure. This effect has recently been demonstrated for breast cancer risk assessment from breast tomosynthesis images.[30] The quantification of JSW with the use of an algorithm like the one described in this paper in conjunction with morphometric analysis of bone trabecular structure has the potential to be a valuable clinical tool for the presence, severity, and progression of OA.

Overall, this study demonstrated preliminary feasibility of quantifying the JSW of the load-bearing knee in tomosynthesis images. A semiautomated algorithm was developed to segment the tibial and femoral edges and quantify the JSW across the knee joint. The resulting JSW map represents a novel method of depicting the three-dimensional characteristics of the knee joint, which may be beneficial for the diagnosis and monitoring of osteoarthritis.

Acknowledgments

The authors thank Dr. Ali Guermazi from Boston University Medical Center for providing the clinical datasets used in this study. The authors also thank the Marquette University Biomedical

Engineering senior design project team that helped design the knee phantom used in this study.

References

1. M. Freedman, J. Hootman, and C. Helmick, "Projected state-specific increases in self-reported doctor-diagnosed arthritis and arthritis-attributable activity limitations–United States, 2005–2030," MMWR Morb Mortal Wkly Rep. **56**, 423–425 (2007) (available URL: http://www.cdc.gov/mmwr/preview/mmwrhtml/mm5617a3.htm).

2. J. Kellgren and J. Lawrence, "Radiological assessment of osteo-arthrosis," Ann. Rheum. Dis. **16**, 494 (1957).http://dx.doi.org/10.1136/ard.16.4.494

3. P. Emrani, J. Katz, C. Kessler, W. Reichmann, E. Wright, T. McAlindon, and E. Losina, "Joint space narrowing and Kellgren-Lawrence progression in knee osteoarthritis: an analytic literature synthesis1," Osteoarthritis Cartilage **16**, 873–882 (2008).http://dx.doi.org/10.1016/j.joca.2007.12.004

4. R. Kijowski, D. G. Blankenbaker, P. T. Stanton, J. P. Fine, and A. A. De Smet, "Radiographic findings of osteoarthritis versus arthroscopic findings of articular cartilage degeneration in the tibiofemoral joint 1," Radiology **239**, 818824 (2006). http://dx.doi.org/10.1148/radiol.2393050584

5. K. A. Beattie, J. Duryea, M. Pui, J. O'Neill, P. Boulos, C. E. Webber, F. Eckstein, and J. D. Adachi, "Minimum joint space width and tibial cartilage morphology in the knees of healthy individuals: A cross-sectional study," BMC Musculoskeletal Disord. 9 (2008).http://dx.doi.org/10.1186/1471-2474-9-119

6. D. Schiphof, M. Boers, and S. Bierma-Zeinstra, "Differences in descriptions of Kellgren and Lawrence grades of knee osteoarthritis," Ann. Rheum. Dis. **67**, 10341036 (2008).http://dx.doi.org/10.1136/ard.2007.079020

7. M. Kothari, A. Guermazi, G. von Ingersleben, Y. Miaux, M. Sieffert, J. E. Block, R. Stevens, and C. G. Peterfy, "Fixed-flexion radiography of the knee provides reproducible joint space width measurements in osteoarthritis," Eur. Radiol. **14**, 1568–1573 (2004).http://dx.doi.org/10.1007/s00330-004-2312-6

8. J. Buckland-Wright, D. Macfarlane, S. Williams, and R. Ward, "Accuracy and precision of joint space width measurements in standard and macroradiographs of osteoarthritic knees," Br. Med. J. **54**, 872880 (1995).

9. J. Schmidt, K. Amrami, A. Manduca, and K. Kaufman, "Semi-automated digital image analysis of joint space width in knee radiographs," Skeletal Radiol. **34**, 639–643 (2005).http://dx.doi.org/10.1007/s00256-005-0908-9

10. L. Shamir, S. M. Ling, W. W. Scott, Jr., A. Bos, N. Orlov, T. J. Macura, D. M. Eckley, L. Ferrucci, and I. G. Goldberg, "X-ray image analysis method for automated detection of osteoarthritis," IEEE Trans. Biomed. Eng. **56**, 407–415 (2009).http://dx.doi.org/10.1109/TBME.2008.2006025

11. J. Duryea, J. Li, C. Peterfy, C. Gordon, and H. Genant, "Trainable rule-based algorithm for the measurement of joint space width in digital radiographic images of the knee," Med. Phys. **27**, 580 (2000).http://dx.doi.org/10.1118/1.598897

12. A. Guermazi, D. J. Hunter, and F. W. Roemer, "Plain radiography and magnetic resonance imaging diagnostics in osteoarthritis: validated staging and scoring," J. Bone Jt. Surg. **91**, 5462 (2009).http://dx.doi.org/10.2106/JBJS.H.01385

13. F. W. Roemer, M. D. Crema, S. Trattnig, and A. Guermazi, "Advances in imaging of osteoarthritis and cartilage," Radiology **260**, 332–354 (2011).http://dx.doi.org/10.1148/radiol.11101359

14. F. Eckstein, F. Cicuttini, J. P. Raynauld, J. Waterton, and C. Peterfy, "Magnetic resonance imaging (MRI) of articular cartilage in knee osteoarthritis (OA): morphological assessment," Osteoarthritis Cartilage **14**, 46–75 (2006).http://dx.doi.org/10.1016/j.joca.2006.02.026

15. T. F. Besier, C. E. Draper, G. E. Gold, G. S. Beaupré, and S. L. Delp, "Patellofemoral joint contact area increases with knee flexion and weight bearing," J. Orthop. Res. **23**, 345–350 (2005).http://dx.doi.org/10.1016/j.orthres.2004.08.003

16. M. Logan, E. Dunstan, J. Robinson, A. Williams, W. Gedroyc, and M. Freeman, "Tibiofemoral kinematics of the anterior cruciate ligament

(ACL)-deficient weightbearing, living knee employing vertical access open "interventional," multiple resonance imaging," Am. J. Sports Med. **32**, 720726 (2004).http://dx.doi.org/10.1177/0095399703258771

17. J. T. Dobbins III, H. P. McAdams, D. J. Godfrey, and C. M. Li, "Digital tomosynthesis of the chest," J. Thorac. Imaging **23**, 8692 (2008).http://dx.doi.org/10.1097/RTI.0b013e318173e162

18. J. T. Dobbins III, H. P. McAdams, J. W. Song, C. M. Li, D. J. Godfrey, D. M. DeLong, S. H. Paik, and S. Martinez-Jimenez, "Digital tomosynthesis of the chest for lung nodule detection: Interim sensitivity results from an ongoing NIH-sponsored trial," Med. Phys. **35**, 25542557 (2008).http://dx.doi.org/10.1118/1.2937277

19. J. Duryea, J. Dobbins III, and J. Lynch, "Digital tomosynthesis of hand joints for arthritis assessment," Med. Phys. **30**, 325333 (2003).http://dx.doi.org/10.1118/1.1543573

20. L. T. Niklason, B. T. Christian, L. E. Niklason, D. B. Kopans, D. E. Castleberry, B. H. Opsahl-Ong, C. E. Landberg, P. J. Slanetz, A. A. Giardino, R. Moore, D. Albagli, M. C. DeJule, P. F. Fitzgerald, D. F. Fobare, B. W. Giambattista, R. F. Kwasnick, J. Liu, S. J. Lubowski, G. E. Possin, J. F. Richotte, C. Y. Wei, and R. F. Wirth, "Digital tomosynthesis in breast imaging," Radiology **205**, 399–406 (1997).

21. M. J. Flynn, R. McGee, and J. Blechinger, "Spatial resolution of x-ray tomosynthesis in relation to computed tomography for coronal/sagittal images of the knee," Proc. SPIE **6510**, 65100D (2007).http://dx.doi.org/10.1117/12.713805

22. G. Langs, P. Peloschek, H. Bischof, and F. Kainberger, "Automatic quantification of joint space narrowing and erosions in rheumatoid arthritis," IEEE Trans. Med. Imaging **28**, 151–164 (2009).http://dx.doi.org/10.1109/TMI.2008.2004401

23. H. Shim, S. Chang, C. Tao, J. H. Wang, C. K. Kwoh, and K. T. Bae, "Knee cartilage: efficient and reproducible segmentation on high-spatial-resolution MR images with the semiautomated graph-cut algorithm method," Radiology **251**, 548556 (2009).http://dx.doi.org/10.1148/radiol.2512081332

24. J. Canny, "A computational approach to edge detection," IEEE Trans. Pattern Anal. Mach. Intell., **8**, 679–698 (1986).http://dx.doi.org/10.1109/TPAMI.1986.4767851

25. T. Deller, K. N. Jabri, J. M. Sabol, X. Ni, G. Avinash, R. Saunders, and R. Uppaluri, "Effect of acquisition parameters on image quality in digital tomosynthesis," Proc. SPIE **6510**, 65101L (2007).http://dx.doi.org/10.1117/12.713777

26. T. Sewell, K. Piacsek, B. Heckel, and J. Sabol, "Accurate joint space quantification in knee osteoarthritis: a digital x-ray tomosynthesis phantom study," Proc. SPIE **7961**, 79615N (2011).http://dx.doi.org/10.1117/12.878768

27. J. Koo, M. Chung, B. Choi, H. Yoon, and J. Sabol, "Small lung nodule size measurement with digital tomosynthesis: accuracy in clinical conditions," 96th Scientific Assembly of the Radiological Society of North America (Chicago, IL, 2010).

28. J. C. Buckland-Wright, J. A. Lynch, and D. G. Macfarlane, "Fractal signature analysis measures cancellous bone organisation in macroradiographs of patients with knee osteoarthritis," Ann. Rheum. Dis. **55**, 749–755 (1996).http://dx.doi.org/10.1136/ard.55.10.749

29. V. B. Kraus, S. Feng, S. Wang, S. White, M. Ainslie, A. Brett, A. Holmes, and H. C. Charles, "Trabecular morphometry by fractal signature analysis is a novel marker of osteoarthritis progression," Arthritis Rheum. **60**, 3711–3722 (2009).http://dx.doi.org/10.1002/art.25012

30. D. Kontos, L. C. Ikejimba, P. R. Bakic, A. B. Troxel, E. F. Conant, and A. D. A. Maidment, "Analysis of parenchymal texture with digital breast tomosynthesis: comparison with digital mammography and implications for cancer risk assessment," Radiology **261**, 80–91 (2011).http://dx.doi.org/10.1148/radiol.11100966